

# Electric field gradient in accurate quantum chemical calculations

Andrei Derevianko<sup>1</sup>, U. C. Perera<sup>1</sup>, Marek Krośnicki<sup>2</sup>, Kamil Nalikowski<sup>2</sup>, H. W. T. Morgan<sup>3</sup>, and Valera Veryazov<sup>4</sup>

<sup>1</sup>Department of Physics, University of Nevada, Reno, Nevada 89557, USA

<sup>2</sup>Institute of Theoretical Physics and Astrophysics, University of Gdańsk, Gdańsk, 80-308, Poland

<sup>3</sup>Department of Chemistry, University of Manchester, Oxford Road, Manchester M13 9PL, UK

<sup>4</sup>Division of Computational Chemistry, Chemical Center, Lund University, P.O. Box 124, SE-221 00 Lund, Sweden

\*Email: valera.veryazov@teokem.lu.se

## Abstract

The electric field gradients (EFGs) at the (non-spherical) nucleus contribute to atomic and molecular hyperfine structure and govern Nuclear Quadrupole Resonance (NQR) and Mossbauer spectra. EFGs provide a highly sensitive probe of local bonding, symmetry, and crystal defect geometry and electronic structure. The EFGs can be obtained from electronic structure calculations and can also be extracted from spectroscopic measurements, thus linking electronic structure theory and spectroscopic observables. In this work, we present a methodological study of EFGs for a range of molecules and crystalline materials, using both periodic boundary condition and embedded cluster models, and compare the results with reported experimental data. We analyse the sensitivity of EFG values to details of the calculations, such as the selection of the model Hamiltonians, basis sets, and the geometries of molecules and crystals. We also address persistent differences in EFG sign conventions and tensor definitions employed in the literature and in widely used quantum chemistry codes. While the EFG sign do not affect zero B-field NQR spectra, they can become critical in Mossbauer spectroscopy or when the quadrupolar interactions are combined with other interactions of the nucleus with the environment. Together, our systematic study results provide practical guidelines for computing, interpreting, and exploiting EFGs as quantitative descriptors of electronic structure and chemical environment.

# 1 Introduction

The Electric Field Gradients (EFGs) measure the inhomogeneity of the electric field generated at a nucleus by the surrounding electronic and nuclear charge distributions.<sup>1</sup> Their practical importance in physics and chemistry stems from their couplings to the electric quadrupole moment of nuclei with spin quantum number  $I \geq 1$ . This quadrupolar interaction lifts the degeneracy of the nuclear spin states, causing a spectroscopically detectable splitting of the resulting energy levels. The size of this splitting is proportional to the nuclear quadrupole coupling constant, which depends is proportional to the principal component  $V_{zz}$  of the EFG tensor. Therefore, the EFG provides a link between experimental observables, e.g. transition frequencies measured in the nuclear quadrupole resonance (NQR) spectroscopy and the theoretical description of the electronic structure and chemical environment of a system.<sup>2–6</sup>

In this work we systematically analyze the factors that affect the computation of EFG values across a range of systems, from the water molecule to transition-metal complexes and crystalline materials. Importantly, our study extends conventional EFG calculations to solid-state systems, where we assess the consistency between periodic-boundary-condition methods and embedded-cluster models. Through this comparison, our aim is to identify both the strengths and the potential practical pitfalls of the embedded-cluster approach in providing accurate EFG predictions.

We (i) benchmark Hartree–Fock, density-functional theory (DFT), and multiconfigurational CASSCF (Complete Active Space Self-Consistent Field) and CASPT2 (Complete Active Space Second-Order Perturbation Theory) EFG calculations against experimental data for representative molecules, using several widely employed quantum-chemical codes; (ii) quantify the sensitivity of numerical EFGs to local structural distortions, basis sets, and correlation treatments; (iii) compare embedded-cluster and periodic DFT calculations for crystalline systems. Such systematic work is essential in gauging theoretical errors.

During our work we encountered discrepancies in EFG sign conventions among several widely used quantum-chemistry packages. Gaussian<sup>7</sup> and Molcas<sup>8</sup> report  $V_{zz}$  values with a sign opposite to that used in ORCA<sup>9</sup> and VASP.<sup>10</sup> This inconsistency complicates direct comparison between studies and hinders meaningful comparison of theoretical and experimental results. The origin of the  $V_{zz}$  sign ambiguity can be traced to the fact that zero- $B$ -field NQR experiments measure transition frequencies between EFG-split nuclear sublevels and therefore cannot determine the sign of  $V_{zz}$  directly.<sup>11</sup> At the same time, the  $V_{zz}$  sign carries important spectroscopic information in other experimental techniques: together with the sign of nuclear quadrupole moment  $Q$ , it determines the ordering of the nuclear-spin sublevels  $|I, M_I\rangle$  (with  $M_I$  denoting the spin projection) and the orientation of the principal EFG axis relative to the local bonding environment.<sup>12</sup> Then Mössbauer spectra generally depend on the sign of  $V_{zz}$ . In this work we reconcile outputs from different

electronic-structure packages by providing a self-contained derivation of the quadrupolar Hamiltonian that explicitly tracks the consequences of differing conventions and tensor definitions.

This paper is organized as follows. Sec. 2 provides a self-contained derivation of the expressions for electric-field gradients and the parametrization of the quadrupole interaction, and discusses the relevant conventions used in the literature. Sec. 3 describes the computational methods employed in this study. In Sec. 4 we present and analyze the results, followed by the conclusions. Unless stated otherwise, we use atomic units  $|e| = \hbar = m_e \equiv 1$  and the Gaussian system of electromagnetic units. We take  $e > 0$  to denote the elementary charge, so that the electron charge is  $-e$ . An atomic unit of the EFG is  $|e|/a_0^3 \approx 97.17 \text{ V}\text{\AA}^{-2}$ , where  $a_0$  is the Bohr radius.

## 2 Electric field gradients and quadrupole interaction

### Model Hamiltonian

The quadrupole interaction Hamiltonian  $H_Q$  describes an interaction of nuclear quadrupole moment  $Q$  with electrostatic fields generated by electrons and nuclei. In classical electrodynamics,<sup>13</sup> such interaction is expressed using quadrupole moment tensor  $Q_{ij}$  and the electric field gradients (EFGs)

$$H_Q = \frac{1}{6} \sum_{ij} Q_{ij} V_{ij}. \quad (1)$$

Here  $V_{ij} \equiv \partial_i \partial_j V(\mathbf{r})$  with  $V(\mathbf{r})$  being the electrostatic potential with its derivatives evaluated at the nucleus. Notice that since the E-field  $\mathbf{E} = -\nabla V(\mathbf{r})$ , the EFG tensor can be also expressed as  $V_{ij} = -\partial_i E_j$ . The EFG tensor is real-valued and symmetric  $V_{ij} = V_{ji}$ . Outside the nucleus the EFG tensor is traceless:  $\nabla^2 V = V_{xx} + V_{yy} + V_{zz} = 0$  due to the Laplace theorem. We are interested in the first-order corrections to the energy of the nucleus due to  $H_Q$ .

Notice that following the literature, while we refer to  $V_{ij} = \partial_i \partial_j V(\mathbf{r})$  as EFG, there is a sign difference with  $\partial_i E_j$ , i.e. with EFG taken literally. Moreover, there are various conventions for parametrizing nuclear quadrupole moments. We will address differences in literature conventions in Sec. 2 as these affect comparisons between various quantum chemistry codes and experimental values.

The electrostatic potential  $V(\mathbf{r})$  at point  $\mathbf{r}$  is given by (in atomic units)

$$V(\mathbf{r}) = \sum_B \frac{Z_B}{|\mathbf{r} - \mathbf{R}_B|} - \sum_k \frac{1}{|\mathbf{r} - \mathbf{r}_k|}, \quad (2)$$

where the first sum runs over all the nuclei with position vectors  $\mathbf{R}_B$  and nuclear charges  $Z_B$ , and the

second sum – over all the electrons. Evaluating the derivatives  $V_{ij} = \frac{\partial^2}{\partial x_i \partial x_j} V(\mathbf{r})$ , we obtain the EFG tensor components at the nucleus  $A$ <sup>14</sup>

$$V_{ij}(\mathbf{R}_A) = \sum_{B \neq A} Z_B \frac{3R_{AB,i}R_{AB,j} - \delta_{ij}R_{AB}^2}{R_{AB}^5} - \langle \Phi_{\text{el}} | \sum_k \frac{3r_{Ak,i}r_{Ak,j} - \delta_{ij}r_{Ak}^2}{r_{Ak}^5} | \Phi_{\text{el}} \rangle. \quad (3)$$

Here  $\mathbf{R}_{AB} = \mathbf{R}_A - \mathbf{R}_B$ ,  $\mathbf{r}_{Ak} = \mathbf{R}_A - \mathbf{r}_k$  and  $\Phi_{\text{el}}$  is the electronic wave function for the given configuration of surrounding nuclei.

Cartesian components of the quadrupole moment tensor are  $Q_{ij} = \int d^3r (3x_i x_j - r^2 \delta_{ij}) \rho(\mathbf{r})$ , where  $\rho(\mathbf{r})$  is the nuclear charge density.<sup>13</sup> With the quadrupole moment tensor being symmetric and traceless, we may introduce rank-2 irreducible tensor operator (ITO)  $\mathbf{Q}^{(2)}$  with spherical components

$$\begin{aligned} Q_0^{(2)} &= Q_{zz}, \\ Q_{\pm 1}^{(2)} &= \mp \sqrt{\frac{2}{3}} (Q_{zx} \pm iQ_{zy}), \\ Q_{\pm 2}^{(2)} &= \sqrt{\frac{1}{6}} (Q_{xx} - Q_{yy} \pm 2iQ_{xy}). \end{aligned} \quad (4)$$

Here and below we use Ref.<sup>15</sup> conventions for angular momenta algebra. Spherical components of the EFG ITO  $\mathbf{V}^{(2)}$  are defined in terms of its Cartesian components  $V_{ij}$  in the same way. Then the quadrupolar interaction can be recast into the manifestly rotationally-invariant form,

$$H_Q = \frac{1}{4} (\mathbf{V}^{(2)} \cdot \mathbf{Q}^{(2)}). \quad (5)$$

Focusing on a sub-space spanned by magnetic nuclear substates  $|I, M_I\rangle$  of a fixed nuclear spin  $I$ ,  $\mathbf{Q}^{(2)} \propto [\mathbf{I} \otimes \mathbf{I}]^{(2)}$ . This is a consequence of the Wigner–Eckart theorem. Here we couple two rank-1 nuclear spin ITOs  $\mathbf{I}$  to form a rank-2 ITO,

$$[\mathbf{I} \otimes \mathbf{I}]_q^{(2)} = \sum_{\mu\nu} C_{1\mu;1\nu}^{2q} I_\mu I_\nu,$$

with  $C_{1\mu;1\nu}^{2q}$  being the Clebsch-Gordan coefficients. Defining the nuclear quadrupole moment  $Q$  as an expectation value of  $Q_{zz}$  in the stretched state,  $Q \equiv \langle I, I | Q_{zz} | I, I \rangle$ ,

$$\mathbf{Q}^{(2)} = \frac{\sqrt{6}Q}{I(2I-1)} [\mathbf{I} \otimes \mathbf{I}]^{(2)}. \quad (6)$$

Inverting Eq. (4), Cartesian components of the nuclear quadrupole tensor can be expressed in terms of

Cartesian components of the nuclear spin operators  $I_i$ ,

$$Q_{ij} = \frac{Q}{2I(2I-1)} \left( 3I_i I_j + 3I_j I_i - 2\delta_{ij} I(I+1) \right). \quad (7)$$

It is worth emphasizing that (7) is *effective* operator acting within a fixed- $I$  manifold spanned by the nuclear magnetic substates  $|\alpha, I, M_I\rangle$ , where  $\alpha$  stands for collection of other nuclear quantum numbers.

The expressions so far have been agnostic to the choice of reference frame. To simplify the expression for  $H_Q$ , one rotates the computational reference frame so that the EFG tensor takes the diagonal form. Then it is fully parameterized by three components  $V'_{x'x'}$ ,  $V'_{y'y'}$ , and  $V'_{z'z'}$ . This is the principal axis frame (PAF). If  $\mathbf{U}$  is the rotation matrix from the computational reference frame to the PAF,  $\mathbf{V}' = \text{diag}(V'_{x'x'}, V'_{y'y'}, V'_{z'z'}) = \mathbf{U}\mathbf{V}\mathbf{U}^T$ . Rotations preserve the trace of the matrix. Thereby,  $V'_{x'x'} + V'_{y'y'} + V'_{z'z'} = 0$ , in agreement with the Laplace theorem. In addition, rotations preserve matrix's eigenvalues,<sup>16</sup> so the resulting diagonal-form EFG tensor  $\mathbf{V}'$  is independent (up to permutation) of the reference frame used in computing its non-PAF components, Eq. (3). The quadrupole interaction in the PAF takes a simple form (c.f. Ref.<sup>17</sup>)

$$H_Q = \frac{Q}{2I(2I-1)} (V_{xx} I_x^2 + V_{yy} I_y^2 + V_{zz} I_z^2), \quad (8)$$

where here and below we drop primes for brevity and  $I_{x,y,z}$  are the PAF components of the nuclear spin operator. To arrive at this result we used Eqs. (1) and (7).

The further literature convention<sup>18</sup> is to re-label the PAF axes so that

$$|V_{zz}| \geq |V_{yy}| \geq |V_{xx}|. \quad (9)$$

Then the quantization axis  $z$  is aligned with the steepest E-field gradient at the nucleus and the  $x$  axis — with the minimal gradient direction. Notice that convention (9) coupled with the Laplace condition implies that the signs of  $V_{yy}$  and  $V_{xx}$  are the same<sup>18</sup> and opposite to that of  $V_{zz}$ :  $\text{sgn}(V_{xx}) = \text{sgn}(V_{yy}) = -\text{sgn}(V_{zz})$ .

With the Laplace condition, Eq. (8) reduces to

$$H_Q = \frac{Q}{4I(2I-1)} V_{zz} [3I_z^2 - I(I+1) + \eta (I_x^2 - I_y^2)], \quad (10)$$

where the asymmetry parameter

$$\eta \equiv (V_{xx} - V_{yy})/V_{zz}. \quad (11)$$

The convention (9) implies that  $0 \leq \eta \leq 1$ , see Ref.<sup>18</sup> We remind the reader that the  $H_Q$  parameteriza-

tion (10) only holds in the principal axis frame where the EFG tensor takes the diagonal form. In practice, to compute the spectroscopically relevant transition frequencies,  $H_Q$  is diagonalized in the fixed nuclear spin  $I$  subspace spanned by magnetic states  $|I, M_I\rangle$ . The resulting energy levels are the spectroscopically relevant quantities. As discussed above, the eigenvalues of  $H_Q$  are independent of the choice of reference frame and parameterization of  $H_Q$ .

## Symmetry properties of EFGs

Spatial symmetries impose constraints on the EFG tensor.<sup>19</sup> For axial coordination, as found in tetragonal or hexagonal lattices,  $V_{xx} = V_{yy} = -\frac{1}{2}V_{zz}$  leading to  $\eta = 0$  so that the EFG tensor is fully parameterized by  $V_{zz}$ . In cubic environments,  $V_{zz} = V_{yy} = V_{xx} = 0$ , eliminating quadrupole splittings altogether and rendering  $\eta$  not only irrelevant but formally undefined. Departures from these extremes quantify deviations from an ideal axial or cubic symmetry in the local electronic environment.

There is an important subtlety associated with Eq. (10) convention. The PAF axes are labelled according to Eq. (9). Specifically, the border case  $|V_{zz}| = |V_{yy}|$  triggers an immediate ambiguity as the  $z$ - and  $y$ -axes are no longer uniquely defined. A specific choice flips the sign of  $V_{zz}$ . Indeed, suppose we carried out computations of the EFG tensor  $V_{ij}$ . Then, as a result of diagonalization, we obtained three eigenvalues,  $A > 0$ ,  $B$ , and  $C$  and corresponding unit eigenvectors  $\hat{e}_A, \hat{e}_B, \hat{e}_C$  specifying the PAF. Since  $V_{ij}$  is traceless,  $A + B + C = 0$ . If  $C = 0$ , then  $B = -A < 0$ . The gradient is minimal along  $\hat{e}_C$  (since  $C = 0$ ), so the convention (9) fixes the  $x$ -axis along  $\hat{e}_C$ , but there is an ambiguity in assigning  $y$  and  $z$  axes due to  $|V_{yy}| = |V_{zz}|$ . If we were to align the  $z$ -axis with  $\hat{e}_A$ ,  $V_{zz} = A > 0$ . But if we were to align the  $z$ -axis with  $\hat{e}_B$ , there is a sudden sign flip in the value of  $V_{zz} = B = -A < 0$ . Formally, this leads to a 100% theoretical error but it is just an artifact of the convention (9). More relevant is the fact that the symmetric  $H_Q$  form (8) remains the same if the axes are relabelled, so all these sign and axes flips are due to the convention (9) and thus are purely artificial.

While the discussed  $V_{xx} = 0$  ( $\eta = 1$ ) case seems superficial, it points to a nonphysical sensitivity of the  $V_{zz}$  *sign* and the PAF quantization axis direction to small values of  $V_{xx}$ . Indeed, if  $V_{xx} \approx 0$ , small changes in nuclear positions in Eq. (3) or computational uncertainties can flip the sign of  $V_{xx}$ , which in turn flips the sign of the principal component  $V_{zz}$ —“the  $V_{xx}$  tail wags the  $V_{zz}$  dog.” To prove this statement, we adopt the parametrization of the previous paragraph but with  $C \neq 0$ . We require that  $|C| \ll |A|$  and  $|B|$ . Then the literature convention fixes  $V_{xx} = C$ . Without loss of generality, pick  $A > 0$ . The EFG being traceless requires  $B = -(A + V_{xx}) \approx -A < 0$ : the two dominant eigenvalues  $A$  and  $B$  are close in their absolute

values but are of opposite signs. Two cases follow:

$$\begin{cases} V_{xx} = C < 0 : & |B| = |A + C| = A - |C| < A \Rightarrow V_{zz} = A > 0, \\ V_{xx} = C > 0 : & |B| = |A + C| = A + C > A \Rightarrow V_{zz} = B = -(A + C) < 0. \end{cases}$$

Thus changing the sign of a small (and, therefore, potentially sensitive to computational uncertainties) component  $V_{xx}$  can flip the sign of the assigned  $V_{zz}$ . In practice, we expect the artificial (convention-induced) sign flips to occur when the anisotropy parameter  $\eta \approx 1$  as in all these cases one eigenvalue is small and the other two are approximately equal but opposite in sign.

To mitigate the enumerated artificial sensitivities, theoretical error bars for EFGs should be ideally stated for energy splittings, since the spectroscopic observables are derived from energies of the EFG-split manifolds. Alternatively, Ref.<sup>20</sup> quantifies EFG errors by combining errors in three individual EFG tensor PAF components  $V_{xx}$ ,  $V_{yy}$ , and  $V_{zz}$ .

## Literature conventions and the importance of the EFG sign

There are several parametrizations of the quadrupole interaction Hamiltonian in the literature complicating the comparisons between different quantum chemistry codes and experiments. We have presented a self-contained derivation that makes our definitions explicit thus avoiding potential ambiguities in interpretation of our numerical results.

One of persistent historical discrepancies arises (especially when comparing the Soviet/Russian and the Western research literature in physics) due to the sign difference between elementary charge  $e > 0$  and the electron charge  $-e$ . To avoid this ambiguity we use the absolute value,  $|e|$ , in our work. Then the electron charge is  $-|e|$ . The atomic unit of charge is defined by setting  $|e| = 1$ . This, in particular, fixes the signs in the expression for electrostatic potential  $V(\mathbf{r})$ , Eq. (2), and thus the signs in the EFG expression (3).

Another issue is the sign of EFG. While we refer to  $V_{ij} = \partial_i \partial_j V(\mathbf{r})$  as EFG, E-field gradient taken literally implies taking  $\partial_i E_j$  as EFG. Since  $E_j = -\partial_j V(\mathbf{r})$ , such literal definition would flip the EFG sign. The asymmetry parameter  $\eta$ , Eq. (11), is invariant with respect to  $V_{ij}$  sign flips. However, the overall sign of the quadrupole interaction does matter. Indeed, one can diagonalize the quadrupolar Hamiltonian in the  $|I, M_I\rangle$  space. In the absence of other couplings to the nuclear spin, EFG splits the nuclear manifold into Kramers pairs.  $V_{zz}$  can be factored out in the diagonalization process. Then flipping the  $V_{zz}$  sign would invert the order of the energy levels inside the EFG-split manifolds.

Some experimental observables are sensitive to the sign of  $V_{zz}$ , whereas others are not. For example, a conventional zero- $B$ -field NQR experiment, which measures intra-manifold transition frequencies, is in-

sensitive to the ordering of the levels; accordingly, the sign of  $V_{zz}$  is irrelevant in this context and cannot be determined uniquely.<sup>11,21</sup> Even so, the sign may be extracted at ultralow temperatures from population differences in the EFG-split manifolds.<sup>12</sup>

The  $V_{zz}$  sign is also relevant in atomic physics, where interactions of electrons with nuclear moments lead to spectroscopically resolvable hyperfine structure.<sup>22</sup>  $H_Q$  determines hyperfine constant  $B \propto QV_{zz}$ , see, for example, electronic structure calculations.<sup>23</sup> There  $H_Q$  is added to magnetic-dipole hyperfine interaction setting the grand scale of hyperfine structure manifold splittings and the sign of  $B$  can be deduced because the ordering of levels relative to known magnetic dipole constants  $A$  is different for  $B > 0$  vs  $B < 0$ . Similar considerations apply to molecules, see, e.g., hyperfine structure analyses for HDO,<sup>24</sup> HMn(CO)<sub>5</sub>,<sup>25</sup> and Co(NO)(CO)<sub>3</sub><sup>26</sup> molecules. For all these molecules the EFG sign is determined unambiguously; we will report EFG calculations for these molecules in Sec. 4.

The inconsistency in the sign convention for the principal component of the EFG tensor,  $V_{zz}$ , unfortunately manifests itself in EFGs computed by different packages. In Sec. 4, we examine output from several packages and find that GAUSSIAN<sup>7</sup> and MOLCAS<sup>27</sup> use the  $V_{zz}$  sign convention opposite to many other widely used codes, including DALTON,<sup>28</sup> ORCA,<sup>9</sup> and VASP<sup>10</sup> (one should note here that VASP also uses an opposite definition of the  $x$ - and  $y$ - components:  $|V_{xx}| > |V_{yy}|$  and accordingly the definition of  $\eta$  is corrected<sup>10</sup>). Ref. 29 compares EFG results from several codes, with a note that “a Gaussian convention” is used to present the data. The goal of our derivation and discussion is to “standardize” the conventions across various codes. All our numerical results reported in the following sections adhere to our explicitly specified conventions.

As to the additional conventions, nuclear (electric) quadrupole moment  $Q$  sometimes includes elementary charge and sometimes it does not, see, e.g., Ref. 21,30 Our starting textbook expression (1) for the quadrupole interaction implies that  $Q_{ij}$  is a multipole moment of the nuclear *charge* density. Thereby, the elementary charge is included in the nuclear moment  $Q$  in our formulas. In practice, this does not cause confusion, as long as the units of  $Q$  are specified.

### 3 Computational methods

With regard to the electronic-structure methods, we distinguish between Hartree–Fock (HF),<sup>31</sup> density-functional theory (DFT),<sup>32</sup> and post–Hartree–Fock approaches.<sup>33</sup> HF employs a single Slater determinant and lacks electron correlation beyond the mean field, whereas DFT incorporates correlation approximately via an exchange–correlation functional. Post-HF methods, in particular multiconfigurational approaches such as CASSCF (Complete Active Space Self-Consistent Field)<sup>34</sup> and CASPT2 (Complete Active Space Second-

Order Perturbation Theory),<sup>35,36</sup> go well beyond both mean-field approximations and DFT. These methods provide a controlled treatment of correlation and are essential when strong correlation or near-degeneracies render single-determinant methods (HF or Kohn–Sham DFT) unreliable, for example in systems with (nearly) degenerate electronic states such as transition-metal complexes or in excited states.

Point defects in solids can be modeled using either periodic-boundary-condition (PBC) DFT or embedded-cluster methods, each with distinct advantages and limitations.<sup>37,38</sup> PBC-DFT imposes periodic boundary conditions on a supercell containing the defect together with several unit cells of the host crystal, enabling a direct treatment of band structure and long-range electrostatics within an extended crystalline environment. Although DFT is rigorously formulated for ground states, its application to excited states is less stringent. In addition, artificial interactions between periodic images of the defect may introduce finite-size effects, necessitating large—and therefore computationally expensive—supercells. In contrast, embedded-cluster calculations treat a finite region around the defect quantum mechanically, typically using wave-function-based methods such as CASSCF or CASPT2,<sup>36</sup> while representing the surrounding crystal through an electrostatic embedding potential. This approach excels at describing strongly correlated localized states, excited-state multiplets, and electronic fine structure; however, it lacks a direct connection to the band structure and requires careful treatment of the cluster boundaries and embedding. In practice, the two approaches are complementary: PBC-DFT provides a physically grounded structural and electrostatic context, whereas embedded-cluster methods offer a chemically accurate description of the local electronic structure at defect sites.

In this work, all embedded-cluster calculations were performed using the MOLCAS 8.6 software package.<sup>8</sup> In this approach,<sup>39</sup> a small region of the crystal—the quantum cluster (QC)—is selected for multiconfigurational treatment. The QC is embedded in a shell of *ab initio* model potentials (AIMPs) optimized for the lattice and is further surrounded by point charges. The AIMP s introduce Coulomb and exchange interactions between the cluster electrons and the crystal environment into the electronic Hamiltonian in a mean-field sense, whereas the point charges reproduce the Madelung potential of the bulk crystal. Within the embedded-cluster method, a multielectron Hamiltonian is constructed only for the QC. As a consequence, the QC may carry a nonzero formal charge. The remaining crystal environment is represented by the AIMP s and point charges, which together compensate the formal charge of the QC.

To compare  $V_{zz}$  sign conventions, we computed EFGs with several widely used quantum chemistry codes. HF and DFT calculations were carried out using MOLCAS,<sup>8</sup> ORCA,<sup>9</sup> and GAUSSIAN<sup>7</sup> packages. DFT–PBC results were obtained with VASP.<sup>10</sup> Finally, CASSCF and CASPT2 multiconfigurational calculations were performed in MOLCAS 8.6.<sup>27</sup>

Basis sets used in this work were all of at least triple- $\zeta$  quality. Details are provided in the Supplementary

Materials. For the MOLCAS and ORCA calculations, scalar-relativistic effects were included via the second-order Douglas–Kroll–Hess (DKH2) Hamiltonian.<sup>40</sup>

## 4 Results and discussion

### Electric field gradients in molecules

As discussed in Sec. 2, different quantum-chemistry codes employ different sign conventions for the EFG. In this section we compare EFG results across several widely used packages in order to identify the sign convention adopted by each of them. In addition, because a range of electronic-structure methods is used in EFG calculations, we assess their accuracy by comparison with experimental data and examine the sensitivity of the computed EFGs to the choice of basis set. To ensure a consistent comparison, we compute EFGs using both periodic-boundary-conditions and molecular codes for the same set of molecular systems.

In this section we focus on the water molecule  $\text{H}_2\text{O}$  and on two carbonyl complexes,  $\text{HMn}(\text{CO})_5$ <sup>25</sup> and  $\text{Co}(\text{NO})(\text{CO})_3$ .<sup>26</sup> The signs of the EFGs in all three systems are unambiguously determined experimentally (see Sec. 2). Water serves as a simple and extensively studied reference system, both experimentally and computationally. The complexes  $\text{HMn}(\text{CO})_5$  and  $\text{Co}(\text{NO})(\text{CO})_3$  were selected because their molecular symmetries,  $C_{4v}$  and  $C_{3v}$ , respectively, imply that  $V_{zz}$  is nonzero while  $\eta \equiv 0$  (see Sec. 2).

Symmetry plays an important role in molecular EFGs. In a planar molecule (e.g., water or benzene), the direction perpendicular to the molecular plane can strongly influence the EFG. In some cases the asymmetry parameter approaches unity,  $\eta \approx 1$ , corresponding to  $|V_{xx}|$  being small and hence  $V_{zz} \approx -V_{yy}$ , as in the water molecule with  $\sigma$  bonds lying in the plane.<sup>14</sup> By contrast, in molecules with highly polarizable  $\pi$  bonds, such as benzene, the asymmetry parameter is close to zero,  $\eta \approx 0$ , reflecting  $V_{xx} \approx V_{yy}$ .<sup>30</sup>

Table 1 summarizes our numerical results for the principal component of the EFG tensor,  $V_{zz}$ , and the corresponding asymmetry parameter  $\eta$ . The values are computed at the specific nuclei indicated in the table. Additional computational details are provided in the Supplementary Materials.

In this table, we also compare theoretical and experimental values. Experimental EFG data for the water molecule were obtained from beam–maser spectroscopy.<sup>24</sup> The quadrupole coupling constants for the  $^{55}\text{Mn}$  and  $^{59}\text{Co}$  nuclei in carbonyl complexes were determined from microwave spectra.<sup>25,26</sup> In many cases, the experiments do not report  $V_{zz}$  directly; instead,  $V_{zz}$  (in  $\text{V}/\text{\AA}^2$ ) can be inferred by converting the reported nuclear quadrupole coupling constants. In NQR spectroscopy, the quadrupole coupling is commonly reported either as the transition frequency  $\nu_Q$  (in MHz) or as the quantity  $eQq$  (also in MHz), where  $q \equiv V_{zz}$ . The relation between the measured quadrupole coupling and the principal component of the EFG tensor is more

Table 1: Principal component  $V_{zz}$  (in  $\text{V}\text{\AA}^{-2}$ ) and asymmetry parameter  $\eta$  of the electric-field-gradient tensor for several molecular systems, calculated at the Hartree–Fock, DFT, CASSCF, and CASPT2 levels of theory. The VASP results are obtained under periodic boundary conditions using large translation vectors. For packages marked with an asterisk (\*), the reported values of  $V_{zz}$  are shown with the sign inverted to ensure consistency with the convention defined in Eq. (3).

Method	Software	H <sub>2</sub> O		HMn(CO) <sub>5</sub>		Co(NO)(CO) <sub>3</sub>		
		<sup>17</sup> O	$V_{zz}$	$\eta$	<sup>55</sup> Mn	$V_{zz}$	$\eta$	<sup>59</sup> Co
<b>HF</b>	Molcas*	-181		0.79	-47	0.00	54	0.00
	Gaussian*	-173		0.79	-49	0.00	49	0.00
	ORCA	-182		0.79	-52	0.00	60	0.00
	VASP	-212		0.75	-49	0.01	—	—
<b>DFT-PBE</b>	Molcas*	-169		0.74	-51	0.00	42	0.00
	Gaussian*	-162		0.75	-55	0.00	41	0.00
	ORCA	-176		0.75	-58	0.00	49	0.00
	VASP	-195		0.71	-48	0.00	37	0.03
<b>CASSCF</b>	Molcas*	-165		0.78	-47	0.00	45	0.00
<b>CASPT2</b>	Molcas*	-165		0.77	-48	0.00	44	0.00
<b>Experiment</b>		-164(2) <sup>a</sup>		0.75(2) <sup>a</sup>	-55(2) <sup>b</sup>	0.00	35(3) <sup>c</sup>	0.00

<sup>a</sup>Reference. <sup>24</sup>

<sup>b</sup>Reference. <sup>25</sup>

<sup>c</sup>Reference. <sup>26</sup>

clear if we define "quadrupole coupling constant"

$$C_q \equiv \frac{eQV_{zz}}{\hbar},$$

then

$$\nu_Q \equiv \frac{3C_q}{2I(2I-1)},$$

where  $e$  is the elementary charge,  $Q$  is the nuclear quadrupole moment, and  $I$  is the nuclear spin. For example, the experimental quadrupole coupling constant for <sup>59</sup>Co in Co(NO)(CO)<sub>3</sub> was reported as 35.14(30) MHz, <sup>26</sup> and for <sup>55</sup>Mn in HMn(CO)<sub>5</sub> as -44.22(2) MHz. <sup>25</sup> The values of the nuclear quadrupole moments employed in this study were adopted from Ref. <sup>41</sup>

We employed several widely used electronic-structure codes and compared the resulting EFGs using the standardized conventions defined in Sec. 2. The ORCA and VASP packages adhere to these conventions, whereas the packages marked with an asterisk (MOLCAS and GAUSSIAN) in Table 1 report  $V_{zz}$  values with the opposite sign; for consistency, we invert their signs in the table. We determined the EFG sign conventions used by directly examining outputs from the enumerated packages. Throughout this and following sections, the sign of  $V_{zz}$  is defined according to the convention used in VASP and ORCA, which is consistent with

our derivation of Sec. 2.

At the Hartree–Fock level, the resulting  $V_{zz}$  values for water molecule overestimate the experimental value by up to 12.6%. However, the computed values across the different computational codes are very similar. The DFT-PBE approach shifts the  $V_{zz}$  values closer to the experimental value, reducing the maximum deviation to 7.1%. A similar improvement is observed for the asymmetry parameter. The accuracy is improved further with multiconfigurational methods CASSCF and CASPT2. Active space for  $\text{H}_2\text{O}$  molecule included 8 electrons in 14 orbitals. Using a PBC code (VASP), we achieved a comparable accuracy for  $\eta$ , however the agreement with experimental  $V_{zz}$  is worse. Other periodic codes, for example ELK,<sup>42</sup> produces a bit more consistent values for water molecule:  $V_{zz} = -162.6 \text{ V \AA}^{-2}$  and  $\eta = 0.8$ . However, it seems that periodic codes in general produces the values for EFG for molecules with a systematic error.

As in the case of the water molecule, the  $V_{zz}$  values for the carbonyl complexes obtained with DFT–PBE are closer to the experimental results than those from the Hartree–Fock method. We expect  $\eta = 0$  for the  $C_{4v}$  ( $\text{HMn}(\text{CO})_5$ ) and  $C_{3v}$  ( $\text{Co}(\text{NO})(\text{CO})_3$ ) complexes. For all molecular methods, including multiconfigurational approaches, the resulting value of the asymmetry parameter is consistently  $\eta = 0$ . In other words, molecular methods preserve underlying molecular symmetry. However, the DFT–PBE (VASP) calculations under periodic boundary conditions result in non-vanishing asymmetry parameter for  $\text{Co}(\text{NO})(\text{CO})_3$ . Hartree–Fock calculation of  $\text{Co}(\text{NO})(\text{CO})_3$  with VASP converges to non-symmetric solution.

On average, the CASPT2 method provides the most reliable values of  $V_{zz}$ , followed by DFT–PBE, which exhibits strong consistency across the molecular codes (MOLCAS, GAUSSIAN, and ORCA) and systematically improves upon the Hartree–Fock results.

## Electric field gradients in embedded cluster calculations

With the multiconfigurational calculations of EFGs tested on molecules, we now extend our analysis to crystalline solids. For this purpose, we use the embedded cluster approach<sup>39</sup> as implemented in MOLCAS, see Sec. 3.

Because embedded clusters emulate bulk solids, they are represented in molecular codes (such as MOLCAS) by structures that are more complex than isolated molecules, a feature that is reflected in the EFG calculations, which include both nuclear and electronic contributions, see Eq. (3). The second term in Eq. (3) contains electronic contributions from the cluster, while the first sum includes sums over all the nuclei in both the cluster and AIMP regions. It is essential that neither the cluster nor the AIMP geometries break the underlying crystal symmetry.

We selected  $^{43}\text{Ca}$  in  $\text{CaF}_2$  and  $^{59}\text{Co}$  in  $\text{LaCoO}_3$  as benchmark systems because their high symmetry

provides a stringent test of how well the crystallographic symmetry is preserved by the embedding procedure. Calcium fluoride crystallizes in a cubic structure and is, from a computational standpoint, relatively simple: the pristine material is an ionic crystal with a large direct band gap and has been extensively benchmarked in embedded-cluster calculations.<sup>39</sup> Its octahedral site symmetry implies that all components of the EFG tensor—and hence the asymmetry parameter  $\eta$ —vanish ( $\eta = 0$ ) at every nuclear site in the lattice. This makes the system particularly suitable for testing whether embedded-cluster methods, in combination with multiconfigurational electronic structure approaches, faithfully preserve the site symmetry and do not produce spurious electric-field gradients in either the electronic or nuclear contributions.

Table 2: Principal component  $V_{zz}$  (in  $\text{V}\text{\AA}^{-2}$ ) and asymmetry parameter  $\eta$  calculated at different nuclear centers for quantum clusters embedded into the  $\text{CaF}_2$  and  $\text{LaCoO}_3$  lattices. Values next to the † are treated as  $\eta = 0$  when the  $V_{xx}$  and  $V_{yy}$  are smaller than  $10^{-1} \text{ V}\text{\AA}^{-2}$ . Calculation carried out with MOLCAS software (the  $V_{ii}$  values were changed to the opposite sign).

Nuclear Center	Chemical Formula	Quantum Cluster	Method	$V_{zz}$ ( $\text{V}/\text{\AA}^2$ )	$\eta$
<sup>43</sup> <b>Ca</b>	$\text{CaF}_2$	$\text{CaF}_8\text{Ca}_{12}^{18+}$	HF	0.0	0.00
			CASSCF (6e,12o)	-0.1	0.00
			CASPT2 (6e,12o)	0.0	0.00
			By symmetry	0.0	0.00
<sup>229</sup> <b>Th</b>	$\text{Th}:(\text{CaF}_2)$	$\text{ThF}_8\text{Ca}_{12}^{20+}$	HF	0.0	0.00
			CASSCF (6e,16o)	0.0	0.00
			CASPT2 (6e,16o)	0.0	0.00
			DFT-PBE	-0.8	0.00
			PBC-DFT-PBE	0.0	0.00
			By symmetry	0.0	0.00
			—	—	—
<sup>59</sup> <b>Co</b>	$\text{LaCoO}_3$	$\text{CoO}_6^{9-}$	HF	-4.6	0.00
			CASSCF (42e,23o)	-7.4	0.00
			CASPT2 (42e,23o)	-7.8	0.00
			LDA+U	-8.8(6) <sup>a</sup>	0.00
			Experiment	$\pm 8.1(8)^b$	0.00

<sup>a</sup>Reference.<sup>43</sup>

<sup>b</sup>Reference.<sup>44</sup>

The results of the EFG calculations for the  $\text{CaF}_8\text{Ca}_{12}^{18+}$  and  $\text{ThF}_8\text{Ca}_{12}^{20+}$  clusters are summarized in Table 2. The clusters are specified as follows: the central atom is listed first, followed by the atoms forming the successive coordination shells, and ending with the formal charge of the quantum cluster (QC). As discussed in Sec. 2, all components of the EFG tensor,  $V_{ii}$ , vanish in cubic lattices as a consequence of symmetry. For the multiconfigurational methods, the active space is indicated in parentheses next to the method label in Table 2; for example, in CASSCF (6e,16o), denotes six active electrons (“6e”) distributed over sixteen active orbitals (“16o”). The CASSCF method yields a vanishing EFG provided that the active space is constructed by including all symmetry-equivalent crystal orbitals originating from the open shells of the Th impurity. The influence of the active-space selection on numerical EFGs will be further discussed

in Sec. 4.

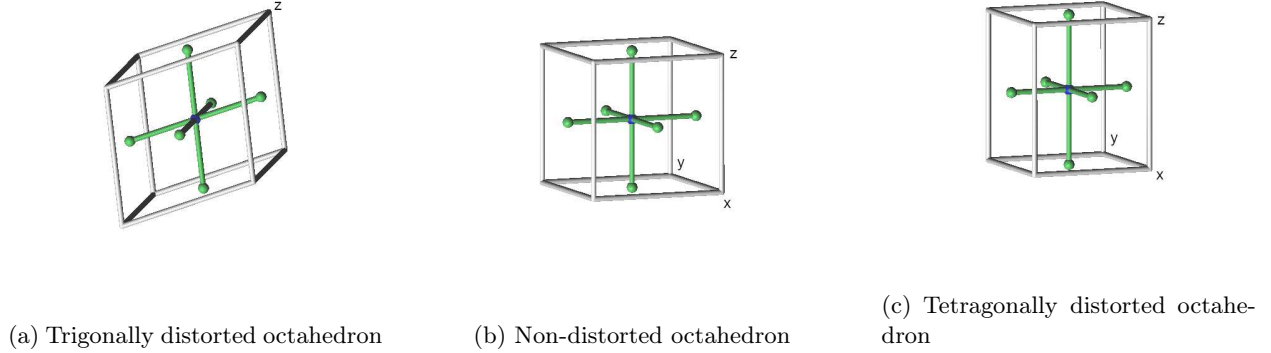


Figure 1: Different symmetry patterns of EFG for octahedrons, shown from left to right: distorted along the  $C_{3v}$  direction (rhombohedral), non-distorted (cubic) and distorted along the  $z$ -direction (tetragonal).

The effects of lattice distortion in the embedded-cluster model are analyzed for the LaCoO<sub>3</sub> crystal, a perovskite-type compound with well-characterized magnetic and electronic properties.<sup>45</sup> LaCoO<sub>3</sub> belongs to the rhombohedral lattice system, and in our calculations we use the experimental geometry parameters reported in Ref. <sup>46</sup> A rhombohedral unit cell can be obtained from the cubic structure by a uniform distortion along the body diagonal coinciding with the  $C_3$  symmetry axis, as illustrated in Fig. 1(c).

By symmetrizing the rhombohedral structure of LaCoO<sub>3</sub>, one can revert it to the corresponding cubic structure, thereby eliminating the contributions of the surrounding ions to the EFG at the Co site, as well as the electronic contributions associated with the local distortion. This provides a convenient framework for testing the sensitivity of the quantum contribution to the EFG with respect to distortions in the local environment of the central Co ion. For the experimental structure, we constructed the embedding and generated the AIMPs and point charges (see Supplementary Materials). The same AIMPs were subsequently used for both the symmetrized (cubic) and experimental (rhombohedral) embeddings. The geometry sensitivity of the EFG will be discussed further in Sec. 4.

The results for the CoO<sub>6</sub><sup>9-</sup> cluster are presented in Table 2. A systematic improvement in the value of  $V_{zz}$  is observed as the level of theory is increased from Hartree–Fock to CASPT2, confirming that the inclusion of electron correlation is essential for reliable prediction of EFGs. The correct value of the asymmetry parameter is preserved in all calculations. In the multiconfigurational treatment, we employed an active space that correlates both the ligand-field electrons and the remaining cobalt  $d$  electrons. This active space comprises 23 orbitals in total: 18 derived from the oxygen  $p$  orbitals and 5 from the cobalt  $d$  orbitals.

Our numerical results for LaCoO<sub>3</sub> are compared to the experimentally deduced value. NMR spec-

troscopy<sup>44</sup> determined the  $^{59}\text{Co}$  ( $I = 7/2$ ) NQR frequency  $\nu_Q$  in a polycrystalline (powder) sample of  $\text{LaCoO}_3$ . In that experiment, a strong externally applied magnetic field defines the quantization axis, so that the Zeeman-split nuclear manifold  $|I, M_I\rangle$  forms the unperturbed basis, while the quadrupole interaction  $H_Q$  can be considered as a perturbation. The powder NMR lines are shifted and broadened by  $H_Q$ , and the value of  $\nu_Q$  is extracted from the second-order (in  $H_Q$ ) corrections to the level energies. Because these corrections scale as  $V_{zz}^2$ , the sign of  $V_{zz}$  cannot be determined unambiguously. Using Eq. (4), we infer an experimental value of  $V_{zz} = \pm 8.1(8) \text{ V}/\text{\AA}^2$ , where the  $\pm$  symbol emphasizes the sign ambiguity. The uncertainty in  $V_{zz}$  is obtained by combining in quadrature the experimental error in  $\nu_Q$  with the uncertainty<sup>30</sup> in the  $^{59}\text{Co}$  nuclear quadrupole moment.

In addition to the experimental comparison, we also compare our EFG values for  $\text{LaCoO}_3$  with the LDA+U (Local Density Approximation with empirical Hubbard correction<sup>47</sup>) result<sup>43</sup>  $V_{zz} = \pm 8.8(6) \text{ V}/\text{\AA}^2$ . Both our ab initio embedded-cluster calculations and the empirical LDA+U results are consistent with the experiment within the quoted uncertainties.

In conclusion, the results of this section demonstrate that the embedding procedure does not, in itself, break the crystal symmetry, which is essential for a correct description of the EFG in solids. In practice, however, both the quantum-cluster region and the AIMP environment must be constructed so as to preserve the underlying symmetry. Furthermore, we find that the accuracy of the calculated nonzero values of  $V_{zz}$  can be systematically improved by increasing the level of electronic-structure treatment. Going beyond the one-electron picture inherent to standard DFT requires particular care; for this reason, the application of multiconfigurational methods to EFG calculations is examined further in Sec. 4.

## Electric Field Gradient sensitivity to the change of geometry

In Sec. 2 we discussed the symmetry properties of the EFG tensor and, in particular, the nonphysical sensitivity of the sign of  $V_{zz}$  to small coordinate perturbations when  $\eta \approx 1$ . Here we illustrate the significance of this observation using the  $\text{H}_2\text{O}$  molecule as a representative example.

The equilibrium H–O–H angle in the water molecule is  $104.5^\circ$ , whereas its transition state is linear (angle  $180^\circ$ ).<sup>48</sup> To analyze the dependence of the asymmetry parameter  $\eta$  on molecular geometry, we varied the bending angle  $\theta$  while keeping the O–H bond length fixed. Fig. 2 shows the principal component of the electric-field gradient,  $V_{zz}$  and the asymmetry parameter  $\eta$  evaluated at the oxygen nucleus as functions of the H–O–H bending angle  $\theta$ .

The principal component  $V_{zz}$  is found to be relatively insensitive to changes in geometry; however, near  $\theta \approx 111^\circ$ , where the asymmetry parameter reaches  $\eta = 1$ , a discontinuous change in the *sign* of  $V_{zz}$  occurs

while its magnitude  $|V_{zz}|$  remains continuous. In the upper panel of Fig. 2,  $V_{zz}$  is shown as closed circles, whereas the absolute value  $|V_{zz}|$  is plotted as open red circles in the region where  $V_{zz} < 0$ . For larger angles,  $\eta$  decreases monotonically and approaches zero as  $\theta \rightarrow 180^\circ$ , where the geometry of  $\text{H}_2\text{O}$  attains cylindrical symmetry about the mol

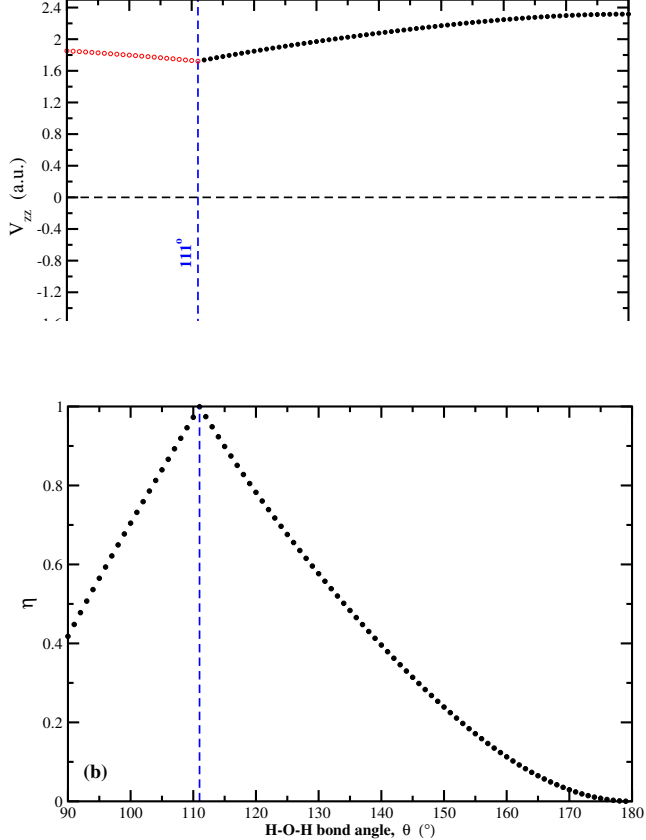


Figure 2: EFG at the oxygen in a water molecule as a function of the H–O–H bond angle,  $\theta$ . Panel (a) shows the principal EFG component  $V_{zz}$  (in a.u.), with solid black circles for  $V_{zz}$  and open red circles for  $|V_{zz}|$ . Panel (b) shows the corresponding asymmetry parameter  $\eta$ . Calculations were performed using Molcas at the Hartree-Fock theory level with the ANO-L-VTZP basis set.

In Sec. 4 we emphasized the importance of testing the robustness of embedded-cluster models in EFG calculations. In particular, one expects that the magnitude  $|V_{zz}|$  at the ion in the quantum cluster (QC) should vary continuously under small displacements of its nearest-neighbor atoms. As a test case, we consider  $\text{LaCoO}_3$ , discussed in the previous section. We begin with the limiting case of  $\text{LaCoO}_3$  structure having cubic symmetry, in which both  $V_{zz}$  and  $\eta$  vanish by symmetry. In this configuration the QC forms an ideal octahedron (see Fig. 1(b)).

Next, we introduce a controlled distortion by varying the lengths  $Z$  of the  $(\text{Co–O})_z$  bonds aligned along the  $z$  axis, resulting in a tetragonal distortion of the QC, see Fig. 1(c). This modification leaves the  $x$  and  $y$  directions unchanged and therefore implies that, in the diagonalized EFG tensor, the components  $V_{xx}$

and  $V_{yy}$  remain equal, so that  $\eta = 0$ . The EFG values calculated at the  $^{59}\text{Co}$  nucleus as a function of the tetragonal distortion are shown in Fig. 3.

For distortions of up to 2% in the  $(\text{Co}-\text{O})_z$  bonds, the  $V_{zz}$  component of the diagonalized EFG tensor varies linearly within a range of approximately  $\pm 10 \text{ V}/\text{\AA}^2$ . For larger deviations from this geometry, the dependence becomes quadratic. Moving the oxygen atoms closer to the Co nucleus (negative  $\Delta Z/Z$ ) affects  $V_{zz}$  more strongly than stretching the bonds, reflecting the fact that the contribution of a point charge to the EFG scales with distance as  $1/r^3$ , c.f. Eq. (3). These results demonstrate that the embedded-cluster approach provides a physically robust environment for EFG calculations, provided that the structural distortions remain small relative to the equilibrium geometry.

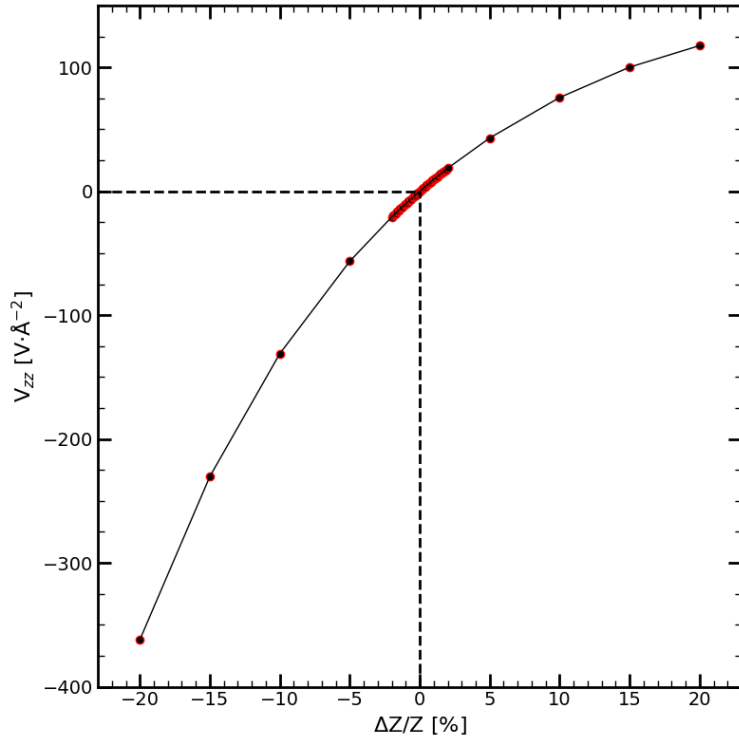


Figure 3: The effect of distortions in the Co–O bond lengths along the  $z$  axis (expressed as a relative change in bond length  $Z$ ) on the principal component  $V_{zz}$  of the electric-field–gradient tensor. This plot is for the symmetrized cubic structure of  $\text{LaCo}_3$ . In all cases the asymmetry parameter vanishes ( $\eta = 0$ ). The calculations were performed at the density-functional-theory level using the PBE functional and the ANO-RCC-VQZP basis set.

## EFG and active space selection

In Sec. 2 we discussed the conditions that must be imposed on the choice of the active space to ensure that multiconfigurational CASSCF calculations preserve symmetry in EFG computations. The selection of the active space is a critical step in any multiconfigurational treatment, as it defines the first-order interaction

Table 3: Active space size and EFG parameters for water molecule and  $\text{ThF}_8\text{Ca}_{12}^{20+}$  cluster. CASSCF calculations were carried out using relativistic basis sets. The number of inactive orbitals and active electrons is reported in the table shown below for each system.

System	Active space size	Correlation Energy, a.u.	Dipole moment, D	$V_{zz}$	$\eta$
$\text{H}_2\text{O}$	HF → 4	0.000	1.98E+00	-181.3	0.79
inactive orbitals: 1	+2 $b_1$ anti-bonding → 5	0.022	1.92E+00	-179.2	0.78
active electrons: 8	+4 $a_1$ anti-bonding → 6	0.054	1.83E+00	-171.0	0.78
	diffuse orbitals begin → 7	0.095	1.78E+00	-163.6	0.81
		8	1.90E+00	-163.2	0.81
		9	1.86E+00	-165.4	0.78
		10	1.88E+00	-166.3	0.77
		11	1.88E+00	-164.9	0.78
		12	1.87E+00	-164.5	0.78
		13	1.89E+00	-164.6	0.77
		14	1.89E+00	-165.0	0.76
$\text{ThF}_8\text{Ca}_{12}^{20+}$	HF → 3	0.000	9.34E-05	0.0	0.00
inactive orbitals: 188	6d-subshell begins → 4	0.007	9.35E-05	-122.3	0.00
active electrons: 6		5	9.37E-05	0.0	0.00
		6	1.45E-04	-89.8	0.00
		7	6.22E-02	-60.3	0.00
	6d-subshell ends → 8	0.070	5.42E-04	0.0	0.00
	7s-subshell → 9	0.073	3.43E-04	0.0	0.00
	5f-subshell begins → 10	0.076	3.38E-02	2.3	0.88
		11	5.71E-02	-11.8	0.54
		12	4.93E-02	15.4	0.90
		13	4.67E-02	26.9	0.16
		14	9.43E-05	6.7	0.00
		15	9.69E-05	0.0	0.00
	5f-subshell ends → 16	0.097	9.50E-05	0.0	0.00

space in which the essential physics of the system is represented. As stated in Sec. 2, the active space must include all symmetry-equivalent orbitals in order to permit their mutual rotations and mixing. In what follows, we explore several alternative active-space choices and demonstrate that, although the correlation energy may improve, symmetry breaking leads to nonphysical EFG results.

Because the choice of basis set has only a minor influence on the EFG parameters (provided that the basis is of sufficient quality, as discussed in the Supplementary Materials), we perform these tests using basis sets of at least TZP quality. Detailed information on the specific basis sets employed is given in the Supplementary Materials.

We begin with the small  $\text{H}_2\text{O}$  molecule, for which we correlate nearly all electrons in the system, leaving only the two electrons occupying the O 1s core orbital inactive. The remaining electrons are distributed among the orbitals that define the active space. The single-determinant Hartree–Fock solution of the electronic Hamiltonian is constructed from four molecular orbitals:  $2a_1$  (primarily O 2s character),  $b_2$  and  $3a_1$  (bonding hybrids of O 2p and H 1s orbitals), and one orbital corresponding to the lone pair.

We then gradually expand the active space by adding one orbital at a time. In successive steps, we include the antibonding  $4a_1$  and  $2b_2$  orbitals, followed by diffuse molecular orbitals with predominant contributions from the O-centered  $s$ ,  $p$ , and  $d$  shells. Table 3 shows the dependence of  $V_{zz}$ ,  $\eta$ , and the electric dipole moment on the construction of the active space. For the water molecule, the correlation energy increases with each additional molecular orbital introduced into the active space, while the dipole moment and the EFG-related quantities converge toward stable values. The most substantial improvement occurs upon inclusion of the first diffuse orbital.

We next consider the  $\text{ThF}_8\text{Ca}_{12}$  cluster embedded in the crystal lattice, modeling a point defect in which a Th impurity substitutes for Ca in  $\text{CaF}_2$  ( $\text{Th}_{\text{Ca}}$  in the Kröger–Vink notation<sup>49</sup>). Understanding  $^{229}\text{Th}$ -doped crystals is essential for the development of solid-state nuclear-clock platforms based on a laser accessible transition in  $^{229}\text{Th}$  nucleus.<sup>50,51</sup> In particular, EFG-split  $^{229}\text{Th}$  manifolds have been spectroscopically resolved in Refs.,<sup>52,53</sup> although the precise nature of the doping sites remains under active discussion.

In the  $\text{ThF}_8\text{Ca}_{12}$  system, the local electronic ground state of the  $\text{Th}^{4+}$  impurity adopts a closed-shell configuration, and the molecular orbitals are predominantly localized on the individual atomic sites. Within the multiconfigurational framework, we therefore select active orbitals that possess primarily single-atom character. We treat as active the six electrons occupying the Th  $6p$  valence subshell, while the inactive space comprises all remaining occupied orbitals of Th, together with the core orbitals of F and Ca and their valence  $p$  subshells. In total, this corresponds to 188 inactive orbitals.

The single-determinant Hartree–Fock solution is constructed from the three Th  $6p$  orbitals. The active orbital space is then systematically enlarged from 3 to 16 orbitals, increasing the size of the configuration space from a single determinant to as many as 157,080 determinants. The additional orbitals introduced into the active space are predominantly Th-centered  $d$ - and  $f$ -type atomic orbitals.

The lower section of Table 3 summarizes the dependence of the EFG-related parameters, the correlation energy, and the dipole moment of the cluster on the choice of active space. The correlation energy (defined as the difference between the total CASSCF and Hartree–Fock energies) increases as additional orbitals are included in the active space; however, this does not necessarily lead to symmetry-consistent values of  $V_{zz}$  and  $\eta$ . Abrupt changes in the dipole moment relative to its Hartree–Fock value indicate that the charge distribution within the cluster has been significantly distorted. Because the charge redistribution is the dominant factor determining the calculated EFGs, deviations from the symmetry-expected values,  $V_{zz} = 0$  and  $\eta = 0$  may arise. We find, see Table 3, that often the errors in calculated  $V_{zz}$  and  $\eta$  are correlated.

When the active space is expanded from 3 to 8 orbitals, an additional Th  $6d$  orbital is added at each step. Inclusion of a single Th  $6d$  orbital breaks the cubic symmetry, whereas inclusion of two such orbitals restores the correct symmetry because they form the  $e_g$  representation of the cubic crystal field. Upon

further enlargement of the active space, the symmetry is again only partially preserved due to mixing of the  $t_{2g}$   $d$  orbitals by the ligand field. Full symmetry is recovered only when the entire  $6d$  subshell—comprising both the  $e_g$  and  $t_{2g}$  manifolds—is included.

Beyond this point, the ninth orbital corresponds to the Th  $7s$  orbital. Subsequent addition of  $f$  orbitals reveals a second pattern of symmetry breaking. For the  $O_h$  point group, the  $f$  orbitals span a seven-dimensional representation that decomposes as

$$\Gamma = A_{2u} \oplus T_{1u} \oplus T_{2u}.$$

When six  $5f$  orbitals (those transforming as  $T_{1u}$  and  $T_{2u}$ ) are included, the results remain consistent with the expected symmetry. A fully symmetry-consistent description is achieved only when all seven  $5f$  orbitals are incorporated into the active space.

To conclude this section, we note that accounting for electron correlation is important for obtaining reliable EFG values. However, while improving electron correlation treatment, one needs to carefully balance contributions from various orbitals spanning the active space to preserve underlying symmetry of the electron charge distribution; it is desirable to include all the orbitals for a given  $\ell$  shell. The dipole moment may serve as a diagnostic of correct symmetry, but it exhibits lower sensitivity compared to  $V_{zz}$  and  $\eta$ . The convergence behavior of the EFG-related parameters with respect to the enlargement of the active space is slow and exhibits a non-monotonic character, as demonstrated by the cluster calculations. Therefore, careful selection of the active space is essential to prevent symmetry breaking in multiconfigurational calculations.

## Conclusions

We have presented a systematic study of electric-field gradients (EFGs) in molecular and solid-state systems using both molecular and periodic electronic-structure codes. Our analysis shows that several widely used computational packages employ opposite sign conventions for the principal component  $V_{zz}$ . We have explicitly documented these convention differences and their impact on reported values. Furthermore, we examined the sensitivity of  $V_{zz}$  and of the asymmetry parameter  $\eta$  to geometric distortions. For all systems studied,  $V_{zz}$  varies continuously and approximately linearly for small distortions away from the equilibrium geometry, with the notable exception of configurations for which  $\eta \approx 1$ . In this regime,  $V_{zz}$  undergoes a sign reversal, so that  $V_{zz}$  is discontinuous while its magnitude  $|V_{zz}|$  remains continuous.

We have verified that the embedded-cluster approach can be reliably employed for the calculation of electric-field gradients in crystalline systems. This proof of concept is particularly important because embedded clusters provide a practical framework for describing local electronic states associated with impurities

or activator ions in a crystal lattice. In addition, we have examined the sensitivity of the EFG to the choice of active space in multiconfigurational calculations. Small molecular systems, in which inner-shell electrons can be explicitly correlated, are found to be less sensitive to active-space selection than embedded clusters containing heavy open-shell elements.

An ion in a crystal experiences a crystal field determined by the lattice symmetry, which lowers the approximate spherical symmetry of the free ion to the point symmetry of the crystallographic site. For the case of thorium embedded in  $\text{CaF}_2$ , we have shown that nonphysical values of  $V_{zz}$  and  $\eta$  arise when one or more orbitals belonging to two- or three-dimensional irreducible representations of the  $O_h$  point group are omitted from the active space. In such cases, the variational CASSCF solution converges to a broken-symmetry wave function. These results indicate that, for embedded clusters and for highly symmetric ligand-field environments, it is generally safer to include all subshell components of the open shell in the active space.

Overall, our results provide practical guidelines for the use of electric field gradients in characterizing electronic structure and local chemical environments, including the selection of an appropriate Hamiltonian and active space, the choice of basis set, the treatment of geometric sensitivity, and the enforcement of consistent sign conventions across computational packages and experimental techniques.

## 5 Acknowledgment

AD thanks Eric Hudson and Danny Rehn for discussions. VV thanks Dr. Adrian M. V. Brânzanic for performing Gaussian calculations. VV thanks Prof. Roland Lindh for a useful hint about implementation of EFG in Molcas. The work of AD and UP was supported in part by the U.S. NSF awards PHY-2207546, PHY-2412869, and PHY-2513134. VV and MK thank Polish National Agency for Academic Exchange under the Strategic Partnership Programme grant BNI/PST/2023/1/00013/U/00001 and grant eSENCE@LU 11:2. This work used Bridges-2 at Pittsburgh Supercomputing Center through allocation PHY230110 from the Advanced Cyberinfrastructure Coordination Ecosystem: Services & Support (ACCESS) program, which is supported by National Science Foundation grants #2138259, #2138286, #2138307, #2137603, and #2138296 and computational resources provided by LUNARC, The Centre for Scientific and Technical Computing at Lund University.

## Supporting information

### 6 Basis sets

All basis sets employed in this study for evaluating the EFG at the selected nuclei were of at least triple-zeta quality. We use a family of atomic natural orbital basis sets with relativistic corrections (ANO-RCC).<sup>54</sup> In Molcas software a use of the ANO basis set family was optimized, particularly for multireference calculations, as it allows for a systematic enhancement of basis set quality. Its application in other quantum chemistry codes is efficient only for relatively small systems. Consequently, we additionally use the def2 basis set family<sup>55</sup> and the aug-cc family,<sup>56</sup> as they are available in all major quantum chemistry packages and provide a comparable level of accuracy for most elements across the periodic table.

The choice of basis sets for different molecular system and methods is presented in Table 4.

In embedded cluster calculations, the primary goal is to describe the electronic structure of the central atom as accurately as possible. This is achieved by using the largest basis set for the central atom while applying smaller basis sets to the surrounding coordination shells, such that the resulting computations remain feasible while only minimally impacting the overall accuracy. Chosen basis sets for distinct atoms in our cluster calculations are presented in Table 5.

Table 4: Basis sets used in EFG calculation for different systems and methods.

Method	Software	System		
		H <sub>2</sub> O	HMn(CO) <sub>5</sub>	CO(NO)(CO) <sub>3</sub>
HF/DFT	Molcas/ORCA	ANO-RCC-VQZP	def2-TZVPP	def2-TZVPP
	Gaussian	aug-cc-pVTZ	aug-cc-pVTZ	aug-cc-pVTZ
CASSCF/CASPT2	Molcas	ANO-RCC-VQZP	ANO-RCC-VQZP	ANO-RCC-VQZP

Table 5: Basis sets used in calculation of EFG in embedded clusters. The boldfaced element represents the central atom of a given cluster. Atomic centers are listed from left to right, beginning with the central atoms, followed by those in the nearest coordination sphere.

System	Cluster	Atomic centers and corresponding bases		
CaF <sub>2</sub>	<b>Ca</b> F <sub>8</sub> Ca <sub>12</sub> <sup>18+</sup>	<b>Ca</b>	F	Ca
		ANO-RCC-VTZ	ANO-RCC-VTZ	ANO-XS-VDZ
Th: CaF <sub>2</sub>	<b>Th</b> F <sub>8</sub> Ca <sub>12</sub> <sup>20+</sup>	<b>Th</b>	F	Ca
		ANO-RCC-VTZP	ANO-RCC-VTZP	ANO-XS-VDZP
LaCoO <sub>3</sub>	<b>Co</b> O <sub>9</sub> <sup>9-</sup>	<b>Co</b>	O	
		ANO-RCC-VQZP	ANO-RCC-VQZP	

## 7 Dependency of EFG in relation to changes of the basis set

We studied dependency of EFG values on the changes in the basis set, see Table 6. For very small and non-physical minimal basis sets, which include only the valence shell, the results are completely wrong. For basis sets of TZ-QZ quality - there is no change in EFG.

Table 6: Effect of **basis set size** on EFG eigenvalues and asymmetry parameter at the **HF** level for H2O.

Family	Label	Basis set contraction for O atom	Energy (Ha)	$V_{zz}$ (V/Å <sup>2</sup> )	$\eta$
ANO-RCC	MB	2S1P	-75.997	325.8	0.939
	VDZ	3S2P	-76.060	-201.7	0.964
	VDZP	3S2P1D	-76.108	-185.3	0.913
	VTZP	4S3P2D1F	-76.117	-174.2	0.927
	VQZP	5S4P3D2F1G	-76.118	-177.6	0.918
ANO-L	MB	2S1P	-75.941	329.7	0.935
	VDZ	3S2P	-76.005	-203.9	0.937
	VDZP	3S2P1D	-76.054	-187.2	0.940
	VTZ	4S3P2D	-76.062	-177.4	0.945
	VTZP	4S3P2D1F	-76.065	-173.9	0.929
	VQZP	5S4P3D2F	-76.066	-177.5	0.939
Pople	6-31G	2S2P	-75.985	-189.9	0.876
	6-31G*	3S2P1D	-76.010	-182.8	0.865
	6-311G**	4S3P1D	-76.046	-193.9	0.924
Slater	STO-3G	2S1P	-74.961	255.3	0.871

## 8 XYZ coordinates of molecules used in the study

12

HMn(CO)5

Mn	0.000000	0.000000	0.1581061
C	0.000000	0.000000	-1.692819
C	0.000000	1.837768	0.378283
C	-1.837768	0.000000	0.378283
C	1.837768	0.000000	0.378283
C	0.000000	-1.837768	0.378283
O	0.000000	0.000000	-2.843221
O	0.000000	2.969319	0.567659
O	-2.969319	0.000000	0.567659
O	2.969319	0.000000	0.567659
O	0.000000	-2.969319	0.567659
H	0.000000	0.000000	1.734176

9

Co(NO)(CO)3

Co	0.000000	0.000000	0.126774
N	0.000000	0.000000	1.785251
C	-0.000357	1.631907	-0.664545
C	1.413452	-0.815645	-0.664545
C	-1.413095	-0.816263	-0.664545
O	0.000000	0.000000	2.945542
O	0.000533	2.678490	-1.135818
O	2.319374	-1.339707	-1.135818
O	-2.319907	-1.338784	-1.135818

## 9 Crystallographic data of structures used in the study

### Calcium Fluoride

Table 7: Unit cell parameters for  $\text{CaF}_2$ .

Formula	$\text{CaF}_2$
Crystal system	Cubic
Space group	$\text{Fm}\bar{3}\text{m}$ (No. 225)
$a$ (Å)	5.51605
$b$ (Å)	5.51605
$c$ (Å)	5.51605
$\alpha = \beta = \gamma$ (°)	90

Table 8: Fractional atomic coordinates for  $\text{CaF}_2$  in space group  $\text{Fm}\bar{3}\text{m}$ .

Atom	$x$	$y$	$z$
Ca (4a)	0	0	0
F (8c)	0.25	0.25	0.25

### Lanthanum Cobaltite

Table 9: Unit cell parameters for  $\text{LaCoO}_3$ .

Formula	$\text{LaCoO}_3$
Crystal system	Rhombohedral
Space group	$\text{R}\bar{3}\text{c}$ (No. 167)
$a$ (Å)	5.34477
$b$ (Å)	5.34477
$c$ (Å)	13.09195
$\alpha = \beta = 90^\circ$ , $\gamma = 120^\circ$	

Table 10: Fractional atomic coordinates for  $\text{LaCoO}_3$  in space group  $\text{R}\bar{3}\text{c}$ .

Atom	Wyckoff	$x$	$y$	$z$
La	6a	0	0	0.25
Co	6b	0	0	0
O	18e	0.55265	0	0.25

## 10 Guide to computing electric field gradients in Molcas

In MOLCAS/OPENMOLCAS, prints the Cartesian components of the EFG tensor, from which the principal component  $V_{zz}$  and the asymmetry parameter  $\eta$  are readily obtained by post-processing.

The EFG tensor  $\mathbf{V}$  is real, symmetric, and traceless. Its principal values  $(V_{xx}, V_{yy}, V_{zz})$  are defined in the principal-axis frame (PAF) with the conventional ordering  $|V_{zz}| \geq |V_{yy}| \geq |V_{xx}|$ , see Sec. 2. The definition of the asymmetry parameter, reproduced here, reads

$$\eta = \frac{V_{xx} - V_{yy}}{V_{zz}}, \quad 0 \leq \eta \leq 1. \quad (12)$$

### Workflow.

1. Increase the Molcas print level (e.g., via `MOLCAS_PRINT=4` or recompile MOLCAS by setting `iPL=4` in `property_util/prop.f`)
2. run `GATEWAY` with `FLDG=0` to print the Cartesian EFG tensor at each nucleus
3. To compute EFG values in CASPT2 level of theory, `DENSITY` keyword should be used.
4. Assemble the symmetric matrix  $\mathbf{V} = \begin{pmatrix} V_{xx} & V_{xy} & V_{xz} \\ V_{xy} & V_{yy} & V_{yz} \\ V_{xz} & V_{yz} & V_{zz} \end{pmatrix}$  from the output. Note that, in MOLCAS implementation, the EFG tensor has the sign opposite to Sec. 2 conventions, so the signs of all components  $V_{ij}$  must be flipped.
5. Diagonalize  $\mathbf{V}$  to obtain eigenvalues; reorder them so that  $|V_{zz}| \geq |V_{yy}| \geq |V_{xx}|$ .
6. Compute  $\eta$  via Eq. (12).

**Illustrative example.** For example, consider the bent H2O molecule with an H–O–H angle of  $\sim 104.5^\circ$ . To extract spectroscopically relevant parameters, one diagonalizes the  $3 \times 3$  tensor to obtain its eigenvalues and eigenvectors, reorders the eigenvalues to satisfy  $|V_{zz}| \geq |V_{yy}| \geq |V_{xx}|$ , and then evaluates  $\eta$  using Eq. (12). We find in atomic units (a.u.),

$$\mathbf{V} = \begin{pmatrix} -1.866 & 0.000 & 0.000 \\ 0.000 & 0.334 & -0.410 \\ 0.000 & -0.410 & 1.542 \end{pmatrix}$$

Diagonalize the reported tensor to obtain its eigenvalues (the principal components)

$$\mathbf{V}_{\text{diag}} = \begin{pmatrix} 1.667 & 0 & 0 \\ 0 & 0.199 & 0 \\ 0 & 0 & -1.866 \end{pmatrix}$$

which remains traceless, as required.

Order the principal components by magnitude according to the standard convention

$$|V_{zz}| > |V_{yy}| > |V_{xx}|.$$

This yields

$$V_{zz} = -1.866, \quad V_{yy} = 1.667, \quad V_{xx} = 0.199 \quad (\text{a.u.}).$$

The dimensionless asymmetry parameter is then

$$\eta = \frac{V_{xx} - V_{yy}}{V_{zz}} = \frac{0.199 - 1.667}{-1.866} \approx 0.767,$$

which satisfies  $0 \leq \eta \leq 1$  by construction.

For unit conversion, one atomic unit of EFG corresponds to  $97.1736243 \text{ V}/\text{\AA}^2$ . Thus  $V_{zz} = -1.866 \text{ a.u.}$  corresponds to  $-181.33 \text{ V}/\text{\AA}^2$ .

## References

- [1] Abragam, A. *The Principles of Nuclear Magnetism*; International series of monographs on physics; Clarendon Press, 1961.
- [2] Suits, B. H. In *Handbook of Applied Solid State Spectroscopy*; Vij, D. R., Ed.; Springer US: Boston, MA, 2006; pp 65–96.
- [3] Wagle, K.; Rehn, D. A.; Mattsson, A. E.; Mason, H. E.; Malone, M. W. *Chemistry of Materials* **2024**, *36*, 7162–7175.
- [4] Errico, L. A.; Cabrera, A. F.; Rentería, M. *Journal of Physical Chemistry C* **2016**, *120*, 21466–21475.
- [5] Choudhary, K.; Faghaninia, A.; Linstrom, R.; Tavazza, F. *Scientific Data* **2020**, *7*, 141.
- [6] Hartman, J. D.; Zhurov, D.; Pinkerton, A. A. *Frontiers in Chemistry* **2021**, *9*, 751711.
- [7] Frisch, M. J.; Trucks, G. W.; Schlegel, H. B.; Scuseria, G. E.; Robb, M. A.; Cheeseman, J. R.; others Gaussian 16 Revision C.01. Gaussian, Inc., Wallingford CT, 2016.
- [8] Aquilante, F. et al. *The Journal of Chemical Physics* **2020**, *152*, 214117.
- [9] Neese, F. *WIREs Comput. Molec. Sci.* **2022**, *12*, e1606.

[10] VASP Software GmbH Vienna Ab initio Simulation Package (VASP). 2023; <https://www.vasp.at>.

[11] Drago, R. S. *Physical methods in Chemistry*; Thomson Learning, 1977.

[12] Pollack, L.; Smith, E. N.; Richardson, R. C. *Journal of Low Temperature Physics* **1997**, *106*, 93–100.

[13] Jackson, J. D. *Classical Electrodynamics*, 3rd ed.; John Wiley and Sons: New York, 1999.

[14] Olsen, L.; Christiansen, O.; Hemmingsen, L.; Sauer, S. P. A.; Mikkelsen, K. V. *J. Chem. Phys.* **2002**, *116*, 1424–1434.

[15] Varshalovich, D. A.; Moskalev, A. N.; Khersonskii, V. K. *Quantum Theory of Angular Momentum*; World Scientific: Singapore, 1988.

[16] Horn, R. A.; Johnson, C. R. *Matrix Analysis*, 2nd ed.; Cambridge University Press: Cambridge, 2013.

[17] Abragam, A. *The Principles of Nuclear Magnetism*; International Series of Monographs on Physics; Oxford University Press: Oxford, 1961; See Chapter “Quadrupole Effects” (pp. 216 ff.) for the derivation of the electric–quadrupole Hamiltonian.

[18] Cohen, M. H.; Reif, F. *Solid State Physics - Advances in Research and Applications* **1957**, *5*, 321–438.

[19] Das, T. P.; Hahn, E. L. *Nuclear Quadrupole Resonance Spectroscopy*; Solid State Physics: Supplement 1; Academic Press: New York, 1958; See Ch. 1 for the EFG tensor,  $V_{xx}+V_{yy}+V_{zz} = 0$  and  $\eta$  ( $0 \leq \eta \leq 1$ ).

[20] Ansari, J. N.; Sauer, K. L.; Glasbrenner, J. K. *Crystals* **2019**, *9*.

[21] Smith, J. A. S. *Journal of Chemical Education* **1971**, *48*, 39.

[22] Johnson, W. R. *Atomic Structure Theory: Lectures on Atomic Physics*; Springer Series on Atomic, Optical, and Plasma Physics; Springer: Berlin, 2007; Vol. 43.

[23] Beloy, K.; Derevianko, A.; Johnson, W. R. *Phys. Rev. A* **2008**, *77*, 12512.

[24] Verhoeven, J.; Dymantts, A.; Bluysen, H. *The Journal of Chemical Physics* **1969**, *50*, 3330–3338.

[25] Kukolich, S. G.; Sickafoose, S. M. *Chemical Physics Letters* **1993**, *215*, 168–172.

[26] Kukolich, S. G.; Roehrig, M. A.; Haubrich, S. T.; Shea, J. A. *The Journal of Chemical Physics* **1991**, *94*, 191–194.

[27] Aquilante, F.; Autschbach, J.; Carlson, R. K.; Chibotaru, L. F.; Delcey, M. G.; De Vico, L.; others *Journal of Computational Chemistry* **2016**, *37*, 506–541.

[28] Aidas, K. et al. *WIREs Computational Molecular Science* **2014**, *4*, 269–284.

[29] Bjornsson, R.; Bühl, M. *Chemical Physics Letters* **2013**, *559*, 112–116.

[30] Pyykko, P. *Molecular Physics* **2008**, *106*, 1965–1974.

[31] Fock, V. *Zeitschrift für Physik* **1930**, *61*, 126–148.

[32] Kohn, W.; Sham, L. J. *Phys. Rev.* **1965**, *140*, A1133–A1138.

[33] Helgaker, T.; Jørgensen, P.; Olsen, J. *Molecular Electronic Structure Theory*; John Wiley & Sons, Ltd: Chichester, England, 2000.

[34] Roos, B. O.; Taylor, P. R.; Sigbahn, P. *Chemical Physics* **1980**, *48*, 157–173.

[35] Andersson, K.; Malmqvist, P. Å.; Roos, B. O.; Sadlej, A. J.; Wolinski, K. *J. Phys. Chem.* **1990**, *94*, 5483–5488.

[36] Roos, B. O.; Lindh, R.; Malmqvist, P. Å.; Veryazov, V.; Widmark, P.-O. *Multiconfigurational Quantum Chemistry*; Wiley & Sons: Hoboken, 2016; pp 1–224.

[37] Catlow, C. R. A., Mackrodt, W. C., Eds. *Computer simulation of solids*; Springer-Verlag Berlin, 1982.

[38] Kaplan, T., Mahanti, S., Eds. *Electronic Properties of Solids Using Cluster Methods (Fundamental Materials Research)*; Springer New York, NY, 2002.

[39] Larsson, E. D.; Krośnicki, M.; Veryazov, V. *Chemical Physics* **2022**, *562*, 111549.

[40] Reiher, M. *Journal of Chemical Physics* **2004**, *121*, 10945–10956.

[41] Stone, N.; Stone, N. *Table of Nuclear Electric Quadrupole Moments*; 2021.

[42] Dewhurst, J. K.; Sharma, S.; Nordström, L.; Cricchio, F.; Gränäs, O.; Gross, E. K. U. Elk version 10.5.16 released. 2025; <https://sourceforge.net/p/elk/news/2025/06/elk-version-10516-released/>.

[43] Hsu, H.; Blaha, P.; Wentzcovitch, R. M.; Leighton, C. *Physical Review B* **2010**, *82*, 100406.

[44] Itoh, M.; Natori, I. <https://doi.org/10.1143/JPSJ.64.970> **2013**, *64*, 970–975.

[45] Rao, C. N.; Rao, G. V. S. *physica status solidi (a)* **1970**, *1*, 597–652.

[46] Radaelli, P. G.; Cheong, S. W. *Physical Review B* **2002**, 094408.

[47] Himmetoglu, B.; Floris, A.; de Gironcoli, S.; Cococcioni, M. *International Journal of Quantum Chemistry* **2014**, *114*, 14–49.

[48] Peng, C.; Ayala, P. Y.; Schlegel, H.; Frisch, M. *Journal of Computational Chemistry* **1996**, *17*, 49–64.

[49] Kröger, F. A. *The Chemistry of Imperfect Crystals*, 2nd ed.; North-Holland: Amsterdam, 1974.

[50] Tiedau, J. et al. *Physical Review Letters* **2024**, *132*, 182501.

[51] Elwell, R.; Schneider, C.; Jeet, J.; Terhune, J. E. S.; Morgan, H. W. T.; Alexandrova, A. N.; Tran Tan, H. B.; Derevianko, A.; Hudson, E. R. *Phys. Rev. Lett.* **2024**, *133*, 013201.

[52] Zhang, C.; Ooi, T.; Higgins, J. S.; Doyle, J. F.; von der Wense, L.; Beeks, K.; Leitner, A.; Kazakov, G. A.; Li, P.; Thirolf, P. G.; Schumm, T.; Ye, J. *Nature* **2024**, *633*, 63–70.

[53] Hiraki, T. et al. *ArXiv* **2025**,

[54] Roos, B. O.; Lindh, R.; Malmqvist, P. Å.; Veryazov, V.; Widmark, P.-O. *Chemical Physics Letters* **2005**, *409*, 295–299.

[55] Weigend, F.; Ahlrichs, R. *Physical Chemistry Chemical Physics* **2005**, *7*, 3297–3305.

[56] Balabanov, N. B.; Peterson, K. A. *Journal of Chemical Physics* **2005**, *123*.